Limits on High-Frequency Gravitational Waves in Planetary Magnetospheres

Tao Liu[1,*] Jing Ren[2,†] and Chen Zhang[1,‡]

[1]*Department of Physics and Jockey Club Institute for Advanced Study, The Hong Kong University of Science and Technology, Hong Kong S.A.R., People's Republic of China*
[2]*Institute of High Energy Physics, Chinese Academy of Sciences, Beijing 100049, People's Republic of China*

High-frequency gravitational waves (HFGWs) carry a wealth of information on the early Universe with a tiny comoving horizon and astronomical objects of small scale but with dense energy. We demonstrate that the nearby planets, such as Earth and Jupiter, can be utilized as a laboratory for detecting the HFGWs. These GWs are then expected to convert to signal photons in the planetary magnetosphere, across the frequency band of astronomical observation. As a proof of concept, we present the first limits from the existing low-Earth-orbit satellite for specific frequency bands and project the sensitivities for the future more-dedicated detections. The first limits from Juno, the latest mission orbiting Jupiter, are also presented. Attributed to the long path of effective GW-photon conversion and the wide angular distribution of signal flux, we find that these limits are highly encouraging, for a broad frequency range including a large portion unexplored before.

Introduction.—The successful detection of gravitational waves (GWs) by the Laser Interferometer Gravitational-Wave Observatory (LIGO) opens up a window to observe the Universe otherwise inaccessible [1]. This has motivated a series of ongoing and to-be-launched projects to detect the GWs with a frequency ranging from $\sim 10^3$ Hz to orders of magnitude below that. Yet, the GWs with a frequency above that could have also been produced in the early cosmological events such as preheating and high-temperature phase transition and the violent astronomical activities of small-scale objects, e.g., merging of primordial black holes and intercommutation of cosmic strings. Thus, detecting high-frequency GWs (HFGWs) is of high scientific value (for a review, see, e.g., [2]).

However, the detection of HFGWs has been significantly less explored than that of low-frequency GWs [3–5]. Because of the shorter wavelength of HFGWs, this task is more challenging. One traditional wisdom is to employ the inverse Gertsenshtein effect [6–11], where the HFGWs are expected to convert to signal photons in an astronomical [12–16] or artificial [17–38] magnetic field. To compensate for the weakness of gravitational coupling, the magnetic field needs to be either strong or distribute broadly in space. Nonetheless, the existing proposals are subject to a variety of weakness, such as relatively

short path for high-efficient conversion [e.g., neutron star (NS) [11]], large uncertainty of cosmic magnetic field strength [15], highly specific detection frequency band (for a recent effort to address this, see Ref. [38]), and narrow angular distribution of signal flux (especially for some laboratory experiments).

Alternatively, in this Letter, we propose to detect the HFGWs using the nearby planets such as Earth and Jupiter as a laboratory, where the GW-photon conversion is expected to occur in their planetary magnetosphere. Because of its relatively big size, the path for the effective conversion in such a laboratory is typically long. Particularly, as to be shown, such an effective conversion can be achieved across the full electromagnetic (EM) frequency band of astronomical observation, ranging from radio waves to PeV photons. Moreover, as the detectors are positioned in the planetary magnetosphere, the stochastic signals can be detected in a wide range of directions. Combining these features creates a new operation space for detecting the HFGWs (for applying the planets to detect dark matter, see, e.g., [39–45]).

As a proof of concept, we consider the satellite-based detectors at low Earth orbit (LEO), with a bird view to the dark side of Earth. Both diffuse sky background and sunshine are expected to be occulted by the Earth then. We will present the first limits for some specific frequency bands and project the sensitivities for the future more-dedicated detection. It is important to note that the variety of detector designs, such as terrestrial versus satellite based, bird view versus bottom view, etc., can have significant impacts on the sensitivities. Therefore, this Letter should be considered as a starting point for more systematic

exploration of the opportunities presented by such a laboratory, rather than a full demonstration of the sensitivity potential of this strategy.

GW-photon conversion probability.—With a WKB approximation, the inverse Gertsenshtein effect is characterized by a mixing matrix [11,46] (see Supplemental Material Sec. A for details [47])

$$\begin{pmatrix} \Delta_\gamma & \Delta_M \\ \Delta_M & 0 \end{pmatrix}. \tag{1}$$

Here $\Delta_M = \frac{1}{2}\kappa B_t$ encodes the GW-photon mixing, with $\kappa = (16\pi G)^{1/2}$ and B_t being the component of external magnetic field **B** transverse to the GW traveling direction. $\Delta_\gamma \approx \Delta_{vac} + \Delta_{pla}$ is the effective photon mass. $\Delta_{vac} = 7\alpha\omega/(90\pi)(B_t/B_c)^2$ denotes the QED vacuum effect, with α the fine-structure constant, ω the angular frequency, and $B_c = m_e^2/e$. $\Delta_{pla} = -m_{pla}^2/(2\omega)$ represents the plasma-mass contribution with $m_{pla}^2 = 4\pi\alpha n_c/m_c$, where n_c and m_c are the number density and invariant mass of charged plasma particles. By diagonalizing this mixing matrix, one can obtain the GW-photon conversion probability in a homogeneous magnetic field [15,55]

$$P = \sin^2(2\Theta)\sin^2\left(\frac{L}{l_{osc}}\right) = (\Delta_M L)^2 \mathrm{sinc}^2\left(\frac{L}{l_{osc}}\right). \tag{2}$$

Here $\Theta = \frac{1}{2}\arcsin(\Delta_M l_{osc})$ and $l_{osc} = 2/(4\Delta_M^2 + \Delta_\gamma^2)^{1/2}$ are the GW-photon mixing angle and oscillation length, respectively. L is the travel distance of GWs in the magnetic field. For a general path from ℓ_0 to ℓ_1, the conversion probability can be evaluated as [11,56]

$$P = \left| \int_{\ell_0}^{\ell_1} d\ell \Delta_M(\ell) \exp\left(-i\int_{\ell_0}^{\ell} d\ell' \Delta_\gamma(\ell')\right) \right|^2. \tag{3}$$

To have a taste, we first evaluate P_0, the conversion probability for a radial path from zero altitude to infinity over the planet equator. We consider the NSs also for reference. The magnetic fields of both can be modeled as a magnetic dipole, with the magnetic axis aligned with the rotation axis. Then they are transverse to the radial path, with $B_t = -B_0(r_0/r)^3$. Here r_0 is radius and B_0 is surface magnetic field strength. We show P_0 as a function of frequency for the Earth, Jupiter, and two benchmark NSs in Fig. 1. Because of their difference in plasma density profile and external magnetic field strength, the curves demonstrate quite different features.

For the planets, the plasma density is described by a barometric formula, which yields an exponentially suppressed plasma mass as r increases. If ω is not too small, we can set $\Delta_\gamma \approx \Delta_{vac}$ and then obtain
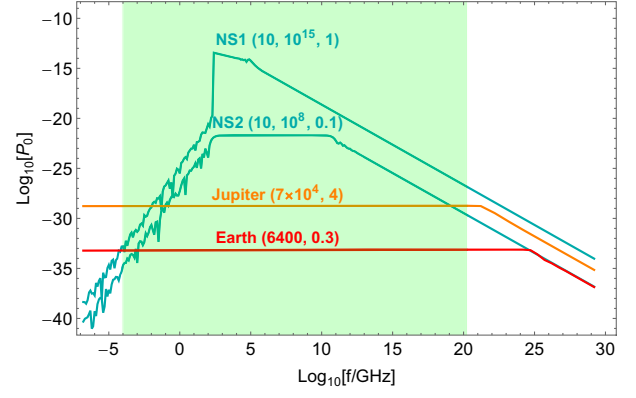
FIG. 1. P_0 as a function of $f = \omega/2\pi$. We show (r_0, B_0) for the planets and $(r_0, B_0, 2\pi/\Omega_{NS})$ for the NSs, where r_0, B_0, and Ω_{NS} (spinning velocity) are in unit of km, Gauss, and second^{-1}, respectively. The green region denotes the EM observation frequency band in astronomy, ranging from radio waves to PeV photons.

$$P_0 = \begin{cases} \frac{1}{4}\Delta_M^2(r_0)r_0^2 \propto B_0^2 r_0^2, & \omega \lesssim \omega_{tra} \\ \frac{1}{4}\Delta_M^2(r_0)r_0^2 \left[\frac{\omega}{\omega_{tra}}\right]^{-\frac{4}{5}} \propto B_0^{\frac{2}{5}} r_0^{\frac{6}{5}} \omega^{-\frac{4}{5}}, & \omega \gtrsim \omega_{tra}, \end{cases} \tag{4}$$

where ω_{tra} is determined by $r_0 \approx l_{osc}(r_0)$, corresponding to the transition point of planet curves in Fig. 1. Consisting with Fig. 1 which is full-calculation based, P_0 is approximately a constant for $\omega \lesssim \omega_{tra}$ and drops as $\propto \omega^{-4/5}$ for $\omega \gtrsim \omega_{tra}$. These relations can be qualitatively explained with Eq. (2). In the homogeneous magnetic field, an optimal probability $P \approx \Delta_M^2 L^2$ can be achieved for $\mathrm{sinc}(L/l_{osc}) \rightarrow 1$ or $l_{osc} \gtrsim L$, a case dubbed as "coherent conversion" [58,59], for given L. When l_{osc} becomes smaller than L, P is suppressed by l_{osc}^2/L^2. Extending this criterion to the planets, we have coherent conversion near their surface for $L \sim r_0 \lesssim l_{osc}(r_0)$ or $\omega \lesssim \omega_{tra}$, where $P_0 \propto \Delta_M^2(r_0)r_0^2 \propto B_0^2 r_0^2$. P_0 for the Jupiter in this region is then $\sim 10^4$ times larger than that of the Earth, as its B_0 and r_0 are both 10 times larger. For $r_0 > l_{osc}(r_0)$, the coherent conversion is suppressed near the planet surface. It can only occur for $r_* \approx l_{osc}(r_*) > r_0$, with a reduced rate $P_0 \sim \Delta_M^2(r_*)r_*^2 \propto B_0^{2/5} r_0^{6/5} \omega^{-4/5}$. As shown in Fig. 1, the frequency band for EM astronomical observations falls entirely into the range of near-surface coherent conversion for both Earth and Jupiter.

In comparison, due to the large strength of their external magnetic field, the NSs tend to have a suppressed l_{osc}. The near-surface coherent conversion thus becomes difficult to achieve. For the two benchmark NSs in Fig. 1, it takes place between 10^2–10^{11} GHz for the NS2, and hardly occurs for the NS1 [60]. In the high-frequency limit, the vacuum effect dominates. P_0 is given by the 2nd formula in Eq. (4). At the low-frequency end, the plasma effect becomes dominant,

yielding a sine-wiggling P_0. With the Goldreich-Julian model for the NS plasma density [61], where $|\Delta_{\text{pla}}| \propto n_c = (2/e)\mathbf{\Omega}_{\text{NS}} \cdot \mathbf{B}[1 - (\Omega_{\text{NS}}r/c)^2\sin^2\theta]^{-1} \propto |\mathbf{B}|$, $|\Delta_{\text{pla}}|$ decays more slowly than Δ_{vac} does as r increases. The coherent conversion then takes place at a larger r_*, compared to the high-frequency case, yielding a more suppressed P_0 as ω decreases [62].

Now let us consider a satellite-based detector positioned at altitude H and latitude $\lambda_{O'}$, and define its instant spherical coordinate system with $\hat{\mathbf{z}}'$ pointing to the planet's center (see Supplemental Material Sec. A for details [47]). Then we are able to evaluate $P(\Omega')$ of HFGWs traveling to this detector in all directions, where $\Omega' = \{\theta', \phi'\}$. Figure 2 displays the θ' dependence of $P(\Omega')$, with $\bar{P}(\theta') = (2\pi P_0)^{-1} \int_0^{2\pi} P(\Omega')d\phi'$. While this figure is drawn with $f = 10^8$ GHz, the features that it demonstrates are almost unchanged for the GW frequency range of interest. Here we neglect the plasma effect which is expected to be small. We split the photon incoming directions into planet-cone (PC) $\{\theta' < \theta_c = \arcsin[r_0/(r_0 + H)]\}$ and outer-space (OS) $(\theta' > \theta_c)$ regions, based on whether the line of sight intersects with planet surface. For all sets of $(H/r_0, \lambda_{O'})$, $\bar{P}(\theta')$ peaks sharply at the PC edge and drops quickly away from it. For $\lambda_{O'} = \pi/2$, it drops all the way to zero at $\theta' = 0$, as B_t vanishes in this direction for a detector right above the planet poles. As H/r_0 increases, with a cost of smaller PC, $\bar{P}(\theta')$ tends to have a bigger value inside the PC due to a longer GW-photon conversion path.

Sensitivity analysis.—The stochastic GWs are typically isotropic and stationary [63]. For a detector in the planetary magnetosphere, we have the GW-converted photon flux (see, e.g., [64])

$$\Phi_\gamma = \int_{\Delta\Omega} d\Omega' \int d\omega \frac{1}{\omega} \frac{d}{d\omega} \frac{d\rho_{\text{GW}}}{d\Omega} P(\Omega'), \qquad (5)$$
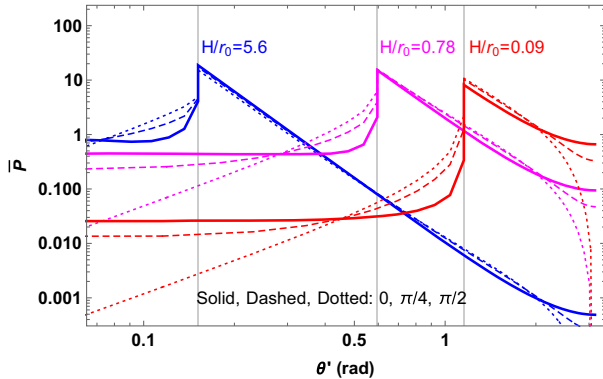
FIG. 2. $\bar{P}(\theta')$ as a function of θ' for a satellite-based detector, with $f = 10^8$ GHz. The color and line style denote the normalized altitude H/r_0 and the latitudes $\lambda_{O'}$ respectively for the satellite. The vertical lines denote θ_c for the PC with different H/r_0 values.

where $\Delta\Omega$ denotes the detector field of view (FOV), $d^2\rho_{\text{GW}}/d\Omega d\ln\omega = \omega^2 h_c^2/(4\pi\kappa^2)$ [63] and h_c is the GW characteristic strain. Note, the angular distribution of GW-converted photons is determined by $P(\Omega')$ and only those falling into the detector FOV can contribute to Φ_γ. The signal and background counts for a narrow frequency band $\Delta\omega$, a short observation time Δt and an effective detector area A are then given by

$$s \approx \Phi_\gamma A\Delta t \approx \frac{h_c^2}{4\pi\kappa^2}\langle P\rangle_{\text{det}} A\Delta t\Delta\omega\Delta\Omega,$$

$$b \approx \Phi_b A\Delta t \approx \phi_b A\Delta t\Delta\omega\Delta\Omega. \qquad (6)$$

Here $\langle P\rangle_{\text{det}} = \int_{\Delta\Omega} P(\Omega')d\Omega'/\Delta\Omega$, essentially determined by the detector position and pointing direction $\{\theta'_{\text{det}}, \phi'_{\text{det}}\}$, denotes the average GW-photon conversion probability over its FOV. If the detector points to the planet center $(\theta'_{\text{det}} = 0)$, $\langle P\rangle_{\text{det}}$ is $\propto \int_{\Delta\Omega} \bar{P}(\theta')\sin\theta' d\theta'/\int_{\Delta\Omega}\sin\theta' d\theta'$ and increases with $\Delta\Omega$ inside the PC. The 95% upper limit on h_c can be derived from $s/\sqrt{b} \approx 1.64$ in the large-background limit:

$$h_{c,95\%} \approx 4.5\kappa\left(\frac{\phi_b}{A\Delta t\Delta\omega\Delta\Omega}\right)^{1/4}\left(\frac{1}{\langle P\rangle_{\text{det}}}\right)^{1/2} \qquad (7)$$

In this Letter, we mainly consider the LEO satellite which has a bird view to the dark side of Earth. With the detector FOV restricted to inside the PC, the dominant backgrounds vary from atmospheric thermal emissions in the infrared (IR) band [65] to cosmic photon albedo (see, e.g., [66]) throughout the optical—γ-ray region. We simplify the analysis by assuming a uniform background flux ϕ_b. We will briefly discuss the Jupiter case also. Given the strong angular dependence of $P(\Omega')$ (see Fig. 2), an efficient detection requires proper design for satellite orbit and full optimization of detector performance. Below let us consider some specific examples.

We first consider the detection of HFGWs in the Earth's magnetosphere. Take the Suzaku mission [67] as an example. The Suzaku has a low inclination orbit (see Table I). It revolves at low latitude and has a performance relatively insensitive to season alternation. Equation (7) thus applies approximately for the entire observation period T_{dark}. Also, as the Suzaku FOV is small, $\langle P\rangle_{\text{det}}$ does not vary much for $\theta'_{\text{det}} \ll \theta_c$. For $\theta'_{\text{det}} = 0$ we have $\langle P\rangle_{\text{det}} \approx 5 \times 10^{-35}$. As for the background flux in the dark side, it has been measured by the Suzaku to be $\phi_b \approx 6.3 \times 10^{-8}$ cm^{-2} s^{-1} keV^{-1} arcmin^{-2} for $\omega \sim 0.5$–10 keV [67]. For one-year operation, we have

$$h_{c,95\%} \sim 2 \times 10^{-25}. \qquad (8)$$

This limit can be scaled to other missions with similar properties, following Eq. (7).

TABLE I. Benchmark scenarios for sensitivity study. For the conservative case, we take the Suzaku-like low inclination orbit [68] with one year operation. The detector FOV and effective area are assumed to be the same as those of the existing missions including Nimbus [69] (IR), Hubble [70,71] (ultraviolet (UV)-Optical), Voyager [72] (extreme UV (EUV)), Suzaku [67] (X-ray) and Fermi-LAT [73] (γ-ray). For the optimistic case, we take the Safir-2-like high inclination orbit [74] with ten year observation. A FOV covering the whole PC is considered. The effective area is set in a way such that the corresponding etendue for the IR, UV-optical, EUV and X-ray bands [75] is consistent with that of future missions [76–79].

	Satellite orbit				Detector properties				
	H (km)	θ_{inc}	T_{dark} (s)		IR	UV-Optical	EUV	X-ray	γ-ray
Conservative	600	31.4°	10^7	$\Delta\Omega$ (sr)	1.6×10^{-2}	10^{-6}	10^{-5}	3×10^{-5}	2.4
				A (cm^2)	0.1225	4.5×10^4	1	250	8000
Optimistic	800	98°	10^8	$\Delta\Omega$ (sr)	3.4	3.4	3.4	3.4	3.4
				A (cm^2)	0.1	10^2	10^2	10^2	10^4

Notably, the satellite at a high inclination orbit has quite different properties. It scans over the high latitude region also, where the conversion probability varies more inside the PC and becomes bigger for a region extending from the PC edge to its inside, compared to the low-latitude case (see Fig. 2). The sensitivity thus could be optimized by taking a detector with either a large FOV covering the whole PC or a small FOV but pointing to the region near the PC edge. Moreover, the observation of such a satellite in the dark side of Earth is sensitive to the season alternation. So we need to generalize Eq. (7) by binning the detector FOV and observation time in this case. The limit shall be obtained from the combined statistics (see Supplemental Material Sec. B for details [47]).

Next, we consider the HFGWs conversion in the Jovian magnetosphere. Take Juno, the latest mission orbiting the giant, as an example. The Juno is settled at a highly elliptical polar orbit with a Perijove ~ 5000 km [80] and a high inclination angle ($\sim 90°$). For each orbit, the Juno spends a few hours around the Perijove in observing the Jupiter's cloud. So Δt is $\sim 10^5$ s for the ~ 35 rounds of its prime mission. As a conservative estimate, we consider the Juno observation of aurora emissions by the Jovian Infrared Auroral Mapper (JIRAM) [81] and UV emissions by the ultraviolet spectrograph (UVS) [82], which set, respectively, $\phi_b \sim 4.2 \times 10^4$ cm^{-2} s^{-1} eV^{-1} arcmin^{-2} for $\omega \sim 0.35$ eV [83] and ~ 34 cm^{-2} s^{-1} eV^{-1} arcmin^{-2} for $\omega \sim 8$ eV [84]. We take $\theta'_{det} \sim 0.8\theta_c$ for $\langle P \rangle_{det}$ and assume $\langle P \rangle_{det}$ to vary little with time. Then, with $\Delta\Omega \sim 10^{-3}$ sr and 3×10^{-4} sr, $A \sim 2$ and 6 cm^2, and $\Delta\omega \sim 1.4 \times 10^{13}$ and 0.9×10^{15} Hz, we have

$$h_{c,95\%} \sim 4 \times 10^{-22} \quad \text{and} \quad 2 \times 10^{-23}, \qquad (9)$$

for the JIRAM and the UVS, respectively.

As a reference, let us consider the conversion of HFGWs in the NS magnetosphere. The NSs are remote. So we have $\langle P \rangle_{det} \sim P_0$ and $\Delta\Omega \sim \pi r_0^2/d^2$, where d is their distance to

the Earth. Take the Magnificent Seven (M7) x-ray dim isolated NSs as an example, which have $d \sim \mathcal{O}(100)$ pc and $B_0 \sim 10^{13}$ G, and hence $P_0 \sim 10^{-18}$ and $\Delta\Omega \sim 10^{-30}$ sr. The PN and MOS of the XMM-Newton telescope have measured the flux of, e.g., J0420 ($d \approx 345$ pc), to be $\phi_b \sim 10^{17}$–10^{19} cm^{-2} s^{-1} keV^{-1} arcmin^{-2} for $\omega \sim 0.5$–1 keV, where $A \sim 1500$ cm^2 and $\Delta t \sim 10^5$ s. Such an intensity consists well with the background model of thermal surface emissions [85]. By applying Eq. (7), we find

$$h_{c,95\%} \sim \mathcal{O}(1) \times 10^{-20}. \qquad (10)$$

Because of the extreme smallness of $\Delta\Omega$, this limit is about 5 orders of magnitude worse than that in Eq. (8). This highlights in part the merit of nearby planets in performing the task of detecting HFGWs.

It is also informative to compare these limits with the ones recast from the existing laboratory experiments for axion detection [24]. In these experiments, the magnetic field is typically confined inside a long straight pipe, with a small cross-sectional area. The GW-photon conversion is suppressed outside the small opening angle of the long pipe. The signal flux in Eq. (5) is thus strongly limited by the detector geometry (see Supplemental Material Sec. C for details [47]). Taking the CERN Axion Solar Telescope (CAST) experiment [86] as an example, we have the recast limit

$$h_{c,95\%} \sim 8 \times 10^{-26}. \qquad (11)$$

Projected sensitivities.—To demonstrate the potential of detecting stochastic HFGWs with the LEO satellites, we define two benchmark scenarios, dubbed "conservative" and "optimistic," in Table I. The choice of orbit in these two scenarios echoes the discussions above on its impacts on the detection efficiency. Figure 3 shows the projected 95% CL limits on the characteristic strain of HFGWs for a
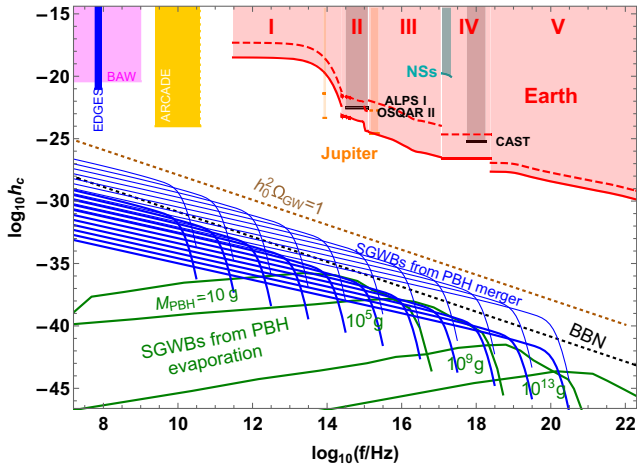
FIG. 3. Projected 95% C.L. upper limits on the characteristic strain h_c of stochastic HFGWs, set by the LEO satellites (red). We estimate these limits with the Suzaku x-ray measurements [67] for band IV, and the IR [65], UV-optical [87–90], EUV [91,92] and γ-ray [93] backgrounds for bands I, II, III, and V, respectively. The dashed and solid bottom lines for these bands correspond to the conservative and optimistic estimates defined in Table I. Moreover, we present the conservative and optimistic limits as orange bands, based on the Juno observation of aurora emissions [83] and UV spectra at Jupiter [84]. We also present the limits set by the x-ray observations of M7 NSs [85] as a cyan band. For completeness, we recast the limits of ALPS, OSQAR and CAST, i.e., three existing laboratory experiments, as gray bands. We denote the highly uncertain radio limits of EDGES and ARCADE [2] as blue and yellow bands [94]. The black dotted line reflects the big bang nucleosynthesis (BBN) constraints on the radiation energy density in the early Universe [95], while the khaki dotted line represents the maximal strain values set by the critical energy density of the Universe today. As a reference, we present the HFGWs from the Hawking evaporation of highly spinning primordial black holes (PBHs) in the early Universe [96–98] as green solid lines, and from the binary mergers of PBHs after the BBN [99] as thin-solid and solid blue lines for two benchmark scenarios. While the former is subject to the BBN constraints, the latter is less restricted.

wide range of frequencies, including a large portion unexplored before.

In the γ-ray band, the limits are strengthened with a rate faster than $\sim f^{-1/2}$, due to the reduction of albedo backgrounds [93]. For the x-ray region, the background flux is taken from the Suzaku measurement. Its conservative limits thus represent the first limits from this mission. For the UV-optical band, we consider the cosmic background [87,88] with a frequency-dependent reflectance of atmosphere [89,90]. The limits get nearly 1 order of magnitude stronger at the right edge of the UV-optical band, due to the ozone absorption of cosmic photons. Such a trend extends to the EUV band, where photodissociation and photoionization become important [100] and a reflectance of $\sim 10^{-3}$ [92] is thus approximately taken for cosmic photons. As for the IR

band, the backgrounds are modeled with a blackbody spectrum at 294 K [65]. These thermal radiations peak at $f \sim 10^{13}$ Hz, and are quickly suppressed for $f > 10^{14}$ Hz. We also present the limits from the observations of Jupiter and NSs in some specific frequency bands. For the optimistic estimate of Jupiter limits, we take $\Delta\Omega = 4$ sr, $A = 100$ cm^2, and $\Delta t = 10^7$ s. Notably, the energy density contribution of GWs with such a large stochastic magnitude at these frequencies is too significant, compared to the BBN constraints and the cosmic critical value today. Nevertheless, the presented limits lay a foundation for further searching for astrophysical signals of, e.g., PBH mergers and advancing detector technologies capable of detecting the signals from the early Universe.

Summary and outlook.—In this Letter, we have proposed to detect the stochastic HFGWs in the planetary magnetosphere. Because of the relatively long path for effective GW-photon conversion, the wide angular distribution of signal flux and a full coverage of the EM observation frequency band in astronomy, this strategy creates a new operation space. With the proof of concept presented, we can immediately see several important directions for next-step explorations.

First, extend the detection of HFGWs from the PC to the OS. As indicated by Fig. 2, the GW-photon conversion probability right outside the PC can be much higher than that inside. Moreover, a detector oriented toward the OS may receive considerably less atmospheric thermal radiation. Second, extend the satellite-based detection to terrestrial observations, which may allow the sensitivities to cover the radio bands. Third, extend the dedicated study to Jupiter and even the Sun, given their stronger magnetic field, larger space for an effective GW-photon conversion, and the active and upcoming missions. We leave these explorations with refined analysis to a paper in preparation [62].

All authors contributed equally to this work.

*taoliu@ust.hk
†renjing@ihep.ac.cn
‡iasczhang@ust.hk

[1] B. P. Abbott *et al.* (LIGO Scientific and Virgo Collaborations), Phys. Rev. Lett. **116**, 061102 (2016).
[2] N. Aggarwal *et al.*, Living Rev. Relativity **24**, 4 (2021).

[3] A. N. Lommen, Rep. Prog. Phys. **78**, 124901 (2015).

[4] C. Tiburzi, Pub. Astron. Soc. Aust. **35**, e013 (2018).

[5] A. I. Renzini, B. Goncharov, A. C. Jenkins, and P. M. Meyers, Galaxies **10**, 34 (2022).

[6] M. Gertsenshtein, Sov. Phys. JETP **14**, 84 (1962).

[7] G. A. Lupanov, Sov. Phys. JETP **25**, 76 (1967), https://ui.adsabs.harvard.edu/abs/1967JETP...25...76L/abstract.

[8] D. Boccaletti, Nuovo Cimento B **70**, 129 (1970).

[9] Y. B. Zeldovich, Sov. Phys. JETP **65**, 1311 (1973), https://ui.adsabs.harvard.edu/abs/1974JETP...38..652Z/abstract.

[10] W. K. De Logi and A. R. Mickelson, Phys. Rev. D **16**, 2915 (1977).

[11] G. Raffelt and L. Stodolsky, Phys. Rev. D **37**, 1237 (1988).

[12] P. Chen, Phys. Rev. Lett. **74**, 634 (1995); **74**, 3091(E) (1995).

[13] A. N. Cillis and D. D. Harari, Phys. Rev. D **54**, 4757 (1996).

[14] M. S. Pshirkov and D. Baskaran, Phys. Rev. D **80**, 042002 (2009).

[15] V. Domcke and C. Garcia-Cely, Phys. Rev. Lett. **126**, 021104 (2021).

[16] S. Ramazanov, R. Samanta, G. Trenkler, and F. R. Urban, J. Cosmol. Astropart. Phys. 06 (2023) 019.

[17] A. Berlin, D. Blas, R. Tito D'Agnolo, S. A. R. Ellis, R. Harnik, Y. Kahn, and J. Schütte-Engel, Phys. Rev. D **105**, 116011 (2022).

[18] O. D. Aguiar, Res. Astron. Astrophys. **11**, 1 (2011).

[19] G. M. Harry, T. R. Stevenson, and H. J. Paik, Phys. Rev. D **54**, 2409 (1996).

[20] N. Herman, A. Füzfa, S. Clesse, and L. Lehoucq, Phys. Rev. D **104**, 023524 (2021).

[21] N. Herman, L. Lehoucq, and A. Fúzfa, Phys. Rev. D **108**, 124009 (2023).

[22] V. Domcke, C. Garcia-Cely, and N. L. Rodd, Phys. Rev. Lett. **129**, 041101 (2022).

[23] A. Ringwald, J. Schütte-Engel, and C. Tamarit, J. Cosmol. Astropart. Phys. 03 (2021) 054.

[24] A. Ejlli, D. Ejlli, A. M. Cruise, G. Pisano, and H. Grote, Eur. Phys. J. C **79**, 1032 (2019).

[25] F.-Y. Li, M.-X. Tang, J. Luo, and Y.-C. Li, Phys. Rev. D **62**, 044018 (2000).

[26] F.-Y. Li, M.-X. Tang, and D.-P. Shi, Phys. Rev. D **67**, 104008 (2003).

[27] F.-Y. Li and N. Yang, Chin. Phys. Lett. **21**, 2113 (2004).

[28] F. Li, R. M. L. Baker, Jr., and Z. Chen, arXiv:gr-qc/0604109.

[29] F. Li, R. M. L. Baker, Jr., Z. Fang, G. V. Stephenson, and Z. Chen, Eur. Phys. J. C **56**, 407 (2008).

[30] M. L. Tong, Y. Zhang, and F. Y. Li, Phys. Rev. D **78**, 024041 (2008).

[31] G. V. Stephenson, AIP Conf. Proc. **1103**, 542 (2009).

[32] F. Li, N. Yang, Z. Fang, R. M. L. Baker, Jr., G. V. Stephenson, and H. Wen, Phys. Rev. D **80**, 064013 (2009).

[33] J. Li, K. Lin, F. Li, and Y. Zhong, Gen. Relativ. Gravit. **43**, 2209 (2011).

[34] F.-Y. Li, H. Wen, and Z.-Y. Fang, Chin. Phys. B **22**, 120402 (2013).

[35] J. Li, L. Zhang, K. Lin, and H. Wen, Int. J. Theor. Phys. **55**, 3506 (2016).

[36] J. Li, L. Zhang, and H. Wen, Int. J. Theor. Phys. **55**, 1871 (2016).

[37] F.-Y. Li, H. Yu, J. Li, L.-F. Wei, and Q.-Q. Jiang, Phys. Rev. D **108**, 065014 (2023).

[38] A. Berlin, D. Blas, R. Tito D'Agnolo, S. A. R. Ellis, R. Harnik, Y. Kahn, J. Schütte-Engel, and M. Wentzel, Phys. Rev. D **108**, 084058 (2023).

[39] K. Zioutas, D. J. Thompson, and E. A. Paschos, Phys. Lett. B **443**, 201 (1998).

[40] H. Davoudiasl and P. Huber, Phys. Rev. Lett. **97**, 141302 (2006).

[41] H. Davoudiasl and P. Huber, J. Cosmol. Astropart. Phys. 08 (2008) 026.

[42] J. L. Feng, J. Smolinsky, and P. Tanedo, Phys. Rev. D **93**, 015014 (2016); **96**, 099901(E) (2017).

[43] R. K. Leane and T. Linden, Phys. Rev. Lett. **131**, 071001 (2023).

[44] L. Li and J. Fan, J. High Energy Phys. 10 (2022) 186.

[45] G. M. French and M. Sher, Phys. Rev. D **106**, 115037 (2022).

[46] D. Ejlli and V. R. Thandlam, Phys. Rev. D **99**, 044022 (2019).

[47] See Supplemental Material at http://link.aps.org/supplemental/10.1103/PhysRevLett.132.131402 for additional calculations and explanations in support of the results presented in this Letter, which includes Refs. [48–54].

[48] K. M. Lee and D. M. Ryan, Phys. Teacher **53**, 122 (2015).

[49] https://nssdc.gsfc.nasa.gov/planetary/factsheet/earthfact.html.

[50] https://nssdc.gsfc.nasa.gov/planetary/factsheet/jupiterfact.html.

[51] C. Dessert, A. J. Long, and B. R. Safdi, Phys. Rev. Lett. **123**, 061104 (2019).

[52] J.-F. Fortin and K. Sinha, J. High Energy Phys. 01 (2019) 163.

[53] J.-F. Fortin, H.-K. Guo, S. P. Harris, E. Sheridan, and K. Sinha, J. Cosmol. Astropart. Phys. 06 (2021) 036.

[54] G. Cowan, K. Cranmer, E. Gross, and O. Vitells, Eur. Phys. J. C **71**, 1554 (2011); **73**, 2501(E) (2013).

[55] I. G. Irastorza and J. Redondo, Prog. Part. Nucl. Phys. **102**, 89 (2018).

[56] Note that in this formalism we have not taken into account the mixing [46] and small difference [11] between the two transverse polarization modes of GW-converted photons, and also their potential mixing with the longitudinal polarization mode [57]. As discussed in Sec. A of the Supplemental Material [47], these effects can be neglected for GW-photon conversion in the planetary magneto-sphere, as the planet magnetic fields are relatively weak and the GW frequencies considered in the later sensitivity analysis are generally high.

[57] A. J. Millar, S. Baum, M. Lawson, and M. C. D. Marsh, J. Cosmol. Astropart. Phys. 11 (2021) 013.

[58] A. Mirizzi and D. Montanino, J. Cosmol. Astropart. Phys. 12 (2009) 004.

[59] A. Kartavtsev, G. Raffelt, and H. Vogel, J. Cosmol. Astropart. Phys. 01 (2017) 024.

[60] For NS1 with $f \sim 10^2$–10^5 GHz, the dominant contribution to P_0 arises from the integration over a specific tiny range of r, where a maximal mixing is achieved with a strong cancellation between Δ_{vac} and Δ_{pla} in Δ_γ.

[61] P. Goldreich and W. H. Julian, Astrophys. J. **157**, 869 (1969).

[62] T. Liu, J. Ren, and C. Zhang (to be published).

[63] J. D. Romano and N. J. Cornish, Living Rev. Relativity **20,** 2 (2017).

[64] M. Leroy, M. Chianese, T. D. P. Edwards, and C. Weniger, Phys. Rev. D **101,** 123003 (2020).

[65] https://www.giss.nasa.gov/research/briefs/2010_schmidt_05/.

[66] M. Turler, M. Chernyakova, T. J. L. Courvoisier, P. Lubinski, A. Neronov, N. Produit, and R. Walter, Astron. Astrophys. **512,** A49 (2010).

[67] K. Koyama, H. Tsunemi, T. Dotani, M. W. Bautz, K. Hayashida, T. G. Tsuru, H. Matsumoto, Y. Ogawara, G. R. Ricker, J. Doty et al., Publ. Astron. Soc. Jpn. **59,** S23 (2007).

[68] https://in-the-sky.org/spacecraft.php?id=28773.

[69] R. Hanel and L. Chaney, NASA Goddard Space Flight Center Document X-650-65-75 (1965).

[70] https://www.nasa.gov/content/observatory-instruments-advanced-camera-for-surveys.

[71] https://www.nasa.gov/mission_pages/hubble/spacecraft/index.html.

[72] A. Broadfoot, B. Sandel, D. Shemansky, S. Atreya, T. Donahue, H. Moos, J.-L. Bertaux, J.-E. Blamont, J. Ajello, D. Strobel et al., Space Sci. Rev. **21,** 183 (1977).

[73] https://fermi.gsfc.nasa.gov/ssc/data/analysis/documentation/Cicerone/Cicerone_Introduction/LAT_overview.html.

[74] https://in-the-sky.org/spacecraft.php?id=25399.

[75] F. Förster et al., Astron. J. **161,** 242 (2021).

[76] https://heasarc.gsfc.nasa.gov/docs/tess/the-tess-space-telescope.html.

[77] N. M. Law, O. Fors, J. Ratzloff, P. Wulfken, D. Kavanaugh, D. J. Sitar, Z. Pruett, M. N. Birchard, B. N. Barlow, K. Cannon et al., Publ. Astron. Soc. Pac. **127,** 234 (2015).

[78] W. YUAN et al., Sci. Sin. Phys. Mech. Astron. **48,** 039502 (2018), https://ui.adsabs.harvard.edu/abs/2018SSPMA.48c9502Y/abstract.

[79] Y. Z. Fan, J. Chang, J. H. Guo, Q. Yuan, Y. M. Hu, X. Li, C. Yue, G. S. Huang, S. B. Liu, C. Q. Feng et al., Acta Astronomica Sinica **63,** 27 (2022), https://ui.adsabs.harvard.edu/abs/2022AcASn..63...27F/abstract.

[80] J. Bloxham, J. E. Connerney, and J. L. Jorgensen, in Proceedings of the AGU Fall Meeting Abstracts (2013), Vol. 2013, p. GP54A–03.

[81] A. Adriani, G. Filacchione, T. Di Iorio, D. Turrini, R. Noschese, A. Cicchetti, D. Grassi, A. Mura, G. Sindoni, M. Zambelli et al., Space Sci. Rev. **213,** 393 (2017).

[82] G. R. Gladstone, S. C. Persyn, J. S. Eterno, B. C. Walther, D. C. Slater, M. W. Davis, M. H. Versteeg, K. B. Persson, M. K. Young, G. J. Dirks et al., Space Sci. Rev. **213,** 447 (2017).

[83] A. Adriani, A. Mura, M. Moriconi, B. Dinelli, F. Fabiano, F. Altieri, G. Sindoni, S. Bolton, J. Connerney, S. Atreya et al., Geophys. Res. Lett. **44,** 4633 (2017).

[84] R. S. Giles, V. Hue, T. K. Greathouse, G. R. Gladstone, J. A. Kammer, M. H. Versteeg, B. Bonfond, D. C. Grodent, J.-C. Gé rard, J. A. Sinclair et al., J. Geophys. Res. **128,** e2022JE007610 (2023).

[85] C. Dessert, J. W. Foster, and B. R. Safdi, Astrophys. J. **904,** 42 (2020).

[86] V. Anastassopoulos et al. (CAST Collaboration), Nat. Phys. **13,** 584 (2017).

[87] M. G. Hauser and E. Dwek, Annu. Rev. Astron. Astrophys. **39,** 249 (2001).

[88] A. Cooray, R. Soc. Open Sci. **3** (2016).

[89] B. R. Scarino, D. R. Doelling, P. Minnis, A. Gopalan, T. Chee, R. Bhatt, C. Lukashin, and C. Haney, IEEE Trans. Geosci. Remote Sens. **54,** 2529 (2016).

[90] L. G. Tilstra, G. van Soest, M. de Graaf, J. R. Acarreta, and P. Stammes, in Atmospheric Chemistry Validation of ENVISA (2004).

[91] R. Hill, K. W. Masui, and D. Scott, Appl. Spectrosc. **72,** 663 (2018).

[92] T. Cravens, J. Clark, A. Bhardwaj, R. Elsner, J. Waite Jr, A. Maurellis, G. Gladstone, and G. Branduardi-Raymont, J. Geophys. Res. **111** (2006).10.1029/2005JA011413.

[93] P. Cumani, M. Hernanz, J. Kiener, V. Tatischeff, and A. Zoglauer, Exp. Astron. **47,** 273 (2019).

[94] As the strength of the cosmic magnetic field is highly unconstrained, these radio limits are subject to a variation of orders of magnitude. While the strongest ones are presented in this figure, it is informative to know that the weakest ones are even weaker than 10^{-14}.

[95] R. H. Cyburt, B. D. Fields, K. A. Olive, and T.-H. Yeh, Rev. Mod. Phys. **88,** 015004 (2016).

[96] R. Anantua, R. Easther, and J. T. Giblin, Phys. Rev. Lett. **103,** 111303 (2009).

[97] A. D. Dolgov and D. Ejlli, Phys. Rev. D **84,** 024028 (2011).

[98] R. Dong, W. H. Kinney, and D. Stojkovic, J. Cosmol. Astropart. Phys. 10 (2016) 034.

[99] G. Franciolini, A. Maharana, and F. Muia, Phys. Rev. D **106,** 103520 (2022).

[100] W. Q. Fu, in Atmospheric Science (Second Edition), edited by J. M. Wallace and P. V. Hobbs (Academic Press, San Diego, 2006), pp. 113–152, ISBN: 978-0-12-732951-2.